Title	High aspect-ratio germanium-tin alloy nanowires: Potential as highly efficient Li-ion battery anodes
Authors	Garcia-Gil, Adrià;Biswas, Subhajit;McNulty, David;Roy, Ahin;Ryan, Kevin M.;Nicolosi, Valeria;Holmes, Justin D.
Publication date	2022-09-07
Original Citation	Garcia-Gil, A., Biswas, S., McNulty, D., Roy, A., Ryan, K. M., Nicolosi, V. and Holmes, J. D. (2022) 'High aspect-ratio germanium-tin alloy nanowires: Potential as highly efficient Li-ion battery anodes', Advanced Materials Interfaces, 9(29), 2201170 (12pp). doi: 10.1002/admi.202201170
Type of publication	Article (peer-reviewed)
Link to publisher's version	https://onlinelibrary.wiley.com/doi/full/10.1002/admi.202201170 - 10.1002/admi.202201170
Rights	© 2022, the Authors. Advanced Materials Interfaces published by Wiley-VCH GmbH. This is an open access article under the terms of the Creative Commons Attribution-NonCommercial-NoDerivs License, which permits use and distribution in any medium, provided the original work is properly cited, the use is non-commercial and no modifications or adaptations are made. - https://creativecommons.org/licenses/by-nc-nd/4.0/
Download date	2024-04-24 13:19:46
Item downloaded from	https://hdl.handle.net/10468/13863

ADVANCED MATERIALS INTERFACES
www.advmatinterfaces.de

High Aspect-ratio Germanium-Tin Alloy Nanowires: Potential as Highly Efficient Li-Ion Battery Anodes

Adrià Garcia-Gil, Subhajit Biswas, David McNulty, Ahin Roy, Kevin M. Ryan, Valeria Nicolosi, and Justin D. Holmes*

Here, the fabrication of a high aspect ratio (>440) $Ge_{1-x}Sn_x$ nanowires with super-thin (≈9 nm) diameter, much below the Bohr radius, using a simple solvothermal-like growth method under supercritical toluene conditions at a reaction temperature of 440 °C is reported. $Ge_{1-x}Sn_x$ nanowires are grown with varying amounts of Sn in Ge lattice, between 3.1 to 10.2 at%. The growth of the $Ge_{1-x}Sn_x$ alloy nanowires is achieved without any additional catalysts, and directly on current collector substrates (titanium) for application as Li-ion battery anodes. The electrochemical performance of the binder-free $Ge_{1-x}Sn_x$ nanowires as an anode material for Li-ion batteries is investigated via galvanostatic cycling and detailed analysis of differential capacity plots. The dimensions of the nanowires, and the amount of Sn in Ge, are critical to achieving a high specific capacity and capacity retention. $Ge_{1-x}Sn_x$ nanowires with the highest aspect ratios and with the lowest Sn content (3.1 at%) demonstrate exceptional capacity retention of ≈90% and 86% from the 10th to the 100th and 150th cycles respectively, while maintaining a very high specific capacity value of 1176 and 1127 mAh g^{-1} after the 100 and 150 cycles respectively.

1. Introduction

Over the past two decades, the growth and properties of $Ge_{1-x}Sn_x$ alloy, mainly in thin-film form, have been extensively studied.[1] Theoretical and experimental studies have depicted a series of interesting features of $Ge_{1-x}Sn_x$ alloys such as higher carrier mobility,[2–4] a tuneable narrow direct bandgap,[5–7] and a low-synthesis temperature (the eutectic point at 231.1 °C) compared to Si and Ge.[8] $Ge_{1-x}Sn_x$ alloys are also deemed to be very versatile and a Si-friendly technology, thus an ideal material for photonics and optoelectronics,[9–16] high-speed field-effect transistors[17,18] and energy storage devices, for example, Li-ion batteries.[19,20]

Li-ion batteries, in particular, claim as a suitable replacement for graphite as an anode material to satisfy the increasing demands for batteries with high power and energy densities.[21,22] Ge and Sn, display higher theoretical capacities than graphite (1620, 991, and 372 mAh g^{-1}, respectively),[23,24] high electrical conductivity, and high Li-ion diffusion at room temperature.[23,25] As a consequence, $Ge_{1-x}Sn_x$ alloys have been put forward as an alternative to graphite for high-specific capacity commercial cells.[19,26,27] The combination of two active Li-ion materials, Ge and Sn, can result in improved conduction paths with high capacity retention, due to the different levels of expansion of Ge and Sn components in the alloy upon lithiation. $Ge_{1-x}Sn_x$ alloy nanostructures have shown improved conduction paths with higher capacity retention and enhanced cycling performance, in comparison with their individual components.[27–30] Further to this, the relative cost of the Ge anode materials could be also reduced by alloying it with cheaper and more abundant elements, such as Sn.

However, the main drawback when using Ge and $Ge_{1-x}Sn_x$ in Li-ion battery anode is the large volume changes encountered upon lithiation/delithiation, which leads to structural cracking and pulverization, resulting in capacity fading and poor cycling life. Nanostructuring (microflowers,[31] nanoparticles,[32] branched nanostructures,[33] nanowires,[20] nanotubes,[34] etc.) of anode materials have been screened to mitigate this obstacle. At the same time, nanowire structures have attracted much attention for Li-ion batteries due to their advantages in providing a 1D conductive path, large specific surface area, short diffusion path of charge carriers (especially thin nanowires), more space

A. Garcia-Gil, S. Biswas, J. D. Holmes
School of Chemistry & Tyndall National Institute
University College Cork
Cork T12 YN60, Ireland
E-mail: s.biswas@ucc.ie

A. Garcia-Gil, S. Biswas, J. D. Holmes
AMBER Centre
Environmental Research Institute
University College Cork
Cork T23 XE10, Ireland

D. McNulty, K. M. Ryan
Bernal Institute & Chemical Sciences Department
University of Limerick
Limerick V94 T9PX, Ireland

A. Roy, V. Nicolosi
School of Chemistry and CRANN
Trinity College Dublin
Dublin 2, Dublin T23 XE10, Ireland

The ORCID identification number(s) for the author(s) of this article can be found under https://doi.org/10.1002/admi.202201170.

DOI: 10.1002/admi.202201170

to buffer volume change and high crack resistance.[35] Nanowire structures are particularly suitable to accommodate high Sn incorporation due to a series of advantages such as strain accommodation due to nanoscale dimensions, and growth at lower reaction temperatures.[36] Thus, developing new, simpler and scalable fabrication methods to tune Sn incorporation in the $Ge_{1-x}Sn_x$ nanostructures and for the generation of long and thin nanowire morphologies for superior electrochemical performances is key for the development of Li-ion battery anodes based on GeSn alloys.[35]

Low-temperature chemical vapor deposition (CVD) and solution-based methods have been employed to synthesize $Ge_{1-x}Sn_x$ nanowires with Sn incorporation in excess of ($x \geq 0.10$) equilibrium concentration of Sn in Ge, primarily deploying metal catalysts.[8,26,37–39] The use of external catalysts can enhance Sn incorporation in Ge nanowires, but can also lead to impurity incorporation from the metallic seeds into the nanowire structure; which can influence the mechanical and electrical properties of the nanowires and potentially the charge capacity of Li-ion cells. Also, the application of $Ge_{1-x}Sn_x$ alloy nanowires in Li-ion batteries is seriously hindered by the tendency for Sn to segregate at high concentrations and the short and tapered morphologies of $Ge_{1-x}Sn_x$ nanowires synthesized, and are not suitable for high-capacity anodes with large capacity retention.[8,28,37,39] Additionally, the necessity for scalability of $Ge_{1-x}Sn_x$ nanowires has placed a different set of demands on synthetic protocols. Thus, the synthesis of long, high-density nanowires grown without any additional catalyst and directly onto the conducting substrates via a simple and scalable method is ideal for the implementation as Li-ion battery anodes.[40]

Here we report, the fabrication of $Ge_{1-x}Sn_x$ ($x \approx 0.03$, 0.08, and 0.10) alloy nanowires using a simple, single-step, solution-based batch synthesis method, without the need for additional catalysts (metal or metalloid) or templates. $Ge_{1-x}Sn_x$ nanowires were synthesized in toluene directly onto Ti metal disc, used as current collectors for Li-ion battery, eliminating the requirement for conductive slurries and binder. The electrochemical performance of the nanowires as Li-ion battery anode was evaluated via long-term galvanostatic cycling. The long $Ge_{1-x}Sn_x$ ($x \approx 0.03$) nanowires exhibited the most impressive electrochemical performance in terms of specific capacity retention, demonstrating a reversible capacity of > 1120 mAh g^{-1} after 150 cycles, which is close to the theoretical capacity of Ge, outperforming all $Ge_{1-x}Sn_x$ nanostructures and most Ge nanowire anodes reported to date.

2. Results and Discussion

For the application of nanomaterials as Li-ion battery anodes, it is key to develop a simple and cost-effective growth process to produce high yields of nanomaterials. The growth of $Ge_{1-x}Sn_x$ alloy nanowires was achieved at 440 °C via a single-step solvothermal-like synthesis method solely in the presence of Ge and Sn precursors, diphenylgermane (DPG), and tetraethyltin (TET) for Ge and Sn respectively, under a supercritical toluene atmosphere (see Supporting Information for detail experimental method). Novel self-seeded growth of $Ge_{1-x}Sn_x$ nanowires was also achieved directly on Ti substrates, which acted as current collectors for Li-ion battery anodes. Closed-cell nanowire growth in a supercritical toluene atmosphere provided ideal conditions for fast precursor decomposition and the formation of high-aspect-ratio 1D nanostructures.

Figure 1a shows a scanning electron microscope (SEM) image of $Ge_{1-x}Sn_x$ nanowires grown on a Ti substrate at a temperature of 440 °C from a DPG/TET (95:5 molar ratio) solution in toluene. Figure 1a,b highlight the formation of high-aspect-ratio nanowires with uniform radial dimensions along their lengths, with lengths of several micrometers (>4 µm). The scanning transmission electron microscopy (STEM) image shown in Figure 1b highlights the detailed nature of the $Ge_{1-x}Sn_x$ nanowires, which display moderate bends and kinks along their lengths. The $Ge_{1-x}Sn_x$ nanowires exhibited a mean diameter of 9.3 (±0.2) nm, evaluation of >100 nanowires, and most of the nanowires exceeded a measurable length over 4 µm (see Figure 1c); giving an aspect ratio of $>4 \times 10^2$. This is the first report of a $Ge_{1-x}Sn_x$ nanowire with a diameter below the Bohr radius of Ge and with an aspect ratio of >100.[1,41] Energy dispersive X-ray (EDX) elemental mapping was performed on $Ge_{1-x}Sn_x$ nanowires to confirm the presence of Sn and the uniformity of Sn dissolution in Ge (see Figure 1d). EDX maps ruled out the formation of any Sn clusters or aggregates in the core or on the surfaces of the nanowires. The uniformity of Sn dissolution in the alloy nanowires was further confirmed by evaluating over 50 nanowires through EDX point scans at different positions along the lengths of the nanowires, obtaining a mean Sn concentration of 3.1 (±1.0) at%. Additionally, contrary to the previously reported $Ge_{1-x}Sn_x$ nanowire growth,[41] no spherical (or hemispherical) growth seeds at the tips of the nanowires were observed, which is typical for catalytic bottom-up growth. The dark-field STEM image shown in Figure 1b confirms the morphology of the nanowires and highlights the absence of growth seeds at the tip of the nanowires.

An increase in the Sn concentration in the nanowires and radically different nanowire morphologies were observed when the Ge:Sn precursor mole ratio was increased from 95:5 to 85:15 (in the reaction solution), keeping the amount (moles) of Ge precursor constant. Average Sn incorporation increased from 3.1 to 7.9 and 10.2 at% with the increase of Sn precursor concentration in the initial solution to 90:10 and 85:15 respectively (see Figure S1a, Supporting Information). Tin distribution and incorporation were also evaluated in high-Sn content nanowires via EDX line-scans and mapping (see Figure S2, Supporting Information). Sn was found to be homogeneously distributed in nanowires with high Sn contents, that is, 10.2 at%, without any Sn segregation. These nanowires also displayed Sn-rich alloy seeds at their tip, suggesting growth through a VLS growth mechanism.

While nanowires grown with a 95:5 (Ge:Sn) mole ratio reaction solution displayed long, thin nanowires with no spherical seeds at their tips (see Figure 1a,b), nanowires grown from 90:10 and 85:15 (Ge:Sn) solution are 5 to 10 times thicker (mean diameters of 48.3 (±2.0) and 108.8 (±2.4) nm) than $Ge_{1-x}Sn_x$ nanowires grown from 95:5 (Ge:Sn) solution. Spherical seeds, typical for catalytic bottom-up growth, were also observed at the tips of these nanowires (see Figure S1b, Supporting Information). These nanowires also revealed appreciable

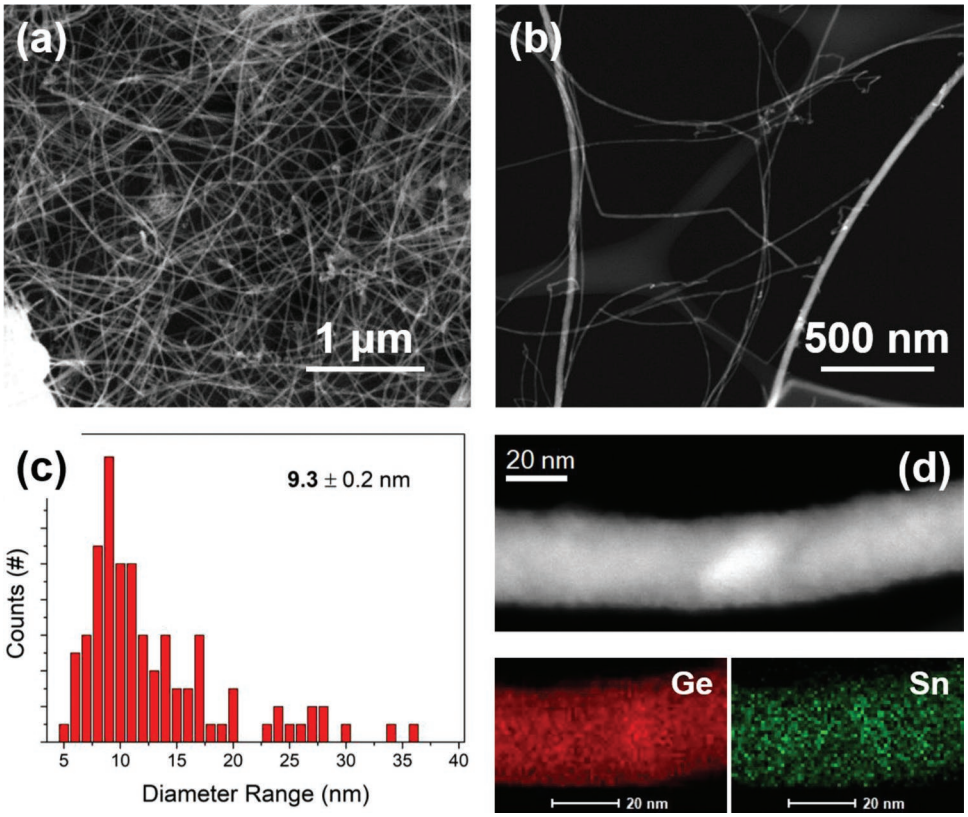

Figure 1. a) SEM image of $Ge_{1-x}Sn_x$ nanowires grown on a Ti substrate from a 95:5 mole ratio of DPG/TET initial solution in toluene at a temperature of 440 °C with a mean Sn content of 3.1 at%. b) A STEM image of the same batch of nanowires as shown in part (a). c) Diameter distribution of the nanowires; showing the mean diameter of 9.3 nm and standard deviation of 0.2. d) HAADF STEM image and corresponding Ge and Sn EDX maps of a single $Ge_{1-x}Sn_x$ nanowire.

inverse tapering along their lengths (see Figure S1b, Supporting Information); up to 100 nm diameter difference along the length of a given nanowire. $Ge_{1-x}Sn_x$ nanowires generated from the 90:10 solution exhibited a mixed morphology of long and uniform nanowires, with the presence of inverse tapered and short nanowires. The amount of inverse tapered nanowires increased and more pronounced tapering was observed in $Ge_{1-x}Sn_x$ nanowires generated from 85:15 $Ge_{1-x}Sn_x$ solution. Tapered nanowires were measured at the base of the seed as a reference diameter value. A radical change in the nanowire morphology with Sn concentrations suggests a very different growth setting with higher amounts of Sn in the initial reaction solution.

2.1. Chemical & Structural Analysis of $Ge_{1-x}Sn_x$ Nanowires

Raman spectroscopy was also used to quantify the Sn inclusion in the $Ge_{1-x}Sn_x$ nanowires. **Figure 2**a shows Raman spectra from $Ge_{1-x}Sn_x$ alloy nanowires with different Sn concentrations. The Ge–Ge LO Raman mode recorded from the nanowires was observed to gradually redshift from bulk Ge[41,42] (303 cm^{-1}), with the LO peak at 298 to 293 cm^{-1} for $Ge_{1-x}Sn_x$ nanowires with 3.1 and 10.2 at% Sn, respectively. A redshift (<5 cm^{-1}) in the Ge–Ge LO mode has previously been reported for phase pure Ge nanowires with diameters <50 nm, in comparison with bulk Ge, due to the phonon confinements effect.[19,42] The Raman shift towards the lower wave numbers in the $Ge_{1-x}Sn_x$ nanowires could therefore be due to both an alloying effect (e.g., mass disorder, bond distortion) and phonon confinement (especially for $Ge_{1-x}Sn_x$ [$x = 0.03$] nanowires with 9.3 nm average diameter); where phonon confinement can also result in the peak broadening. As all Raman measurements were performed at room temperature and low laser power, the peak shift and broadening observed for the $Ge_{1-x}Sn_x$ nanowires were not due to the sample heating. The largest Raman shift was observed for the thickest nanowires (mean diameter of 108.8 nm) with the highest Sn incorporation (10.2 at%) along with the maximum broadening (FWHM of 14.2 cm^{-1}). The presence of any compressive or tensile strain in the nanowires is unlikely, as strain is efficiently released in high surface area structures.[43] While comparison with pure Ge nanowires might be advantageous, similar growth conditions without Sn incorporation yielded Ge nanowires with completely different sizes and morphologies. Additionally, an asymmetry in the lower energy side of the Ge–Ge LO mode was observed in the spectra (especially for the nanowires with higher Sn content) due to the development of a Ge–Sn couple vibrational mode with increasing Sn concentration.[44]

Li et al.[44] introduced a linear expression ($\omega(x) = \omega_0 + \Delta\omega x$) for $Ge_{1-x}Sn_x$ alloy to correlate Sn concentration with the Raman peak shit, obtaining a value of $\Delta\omega = -68$ (± 5) cm^{-1}, while

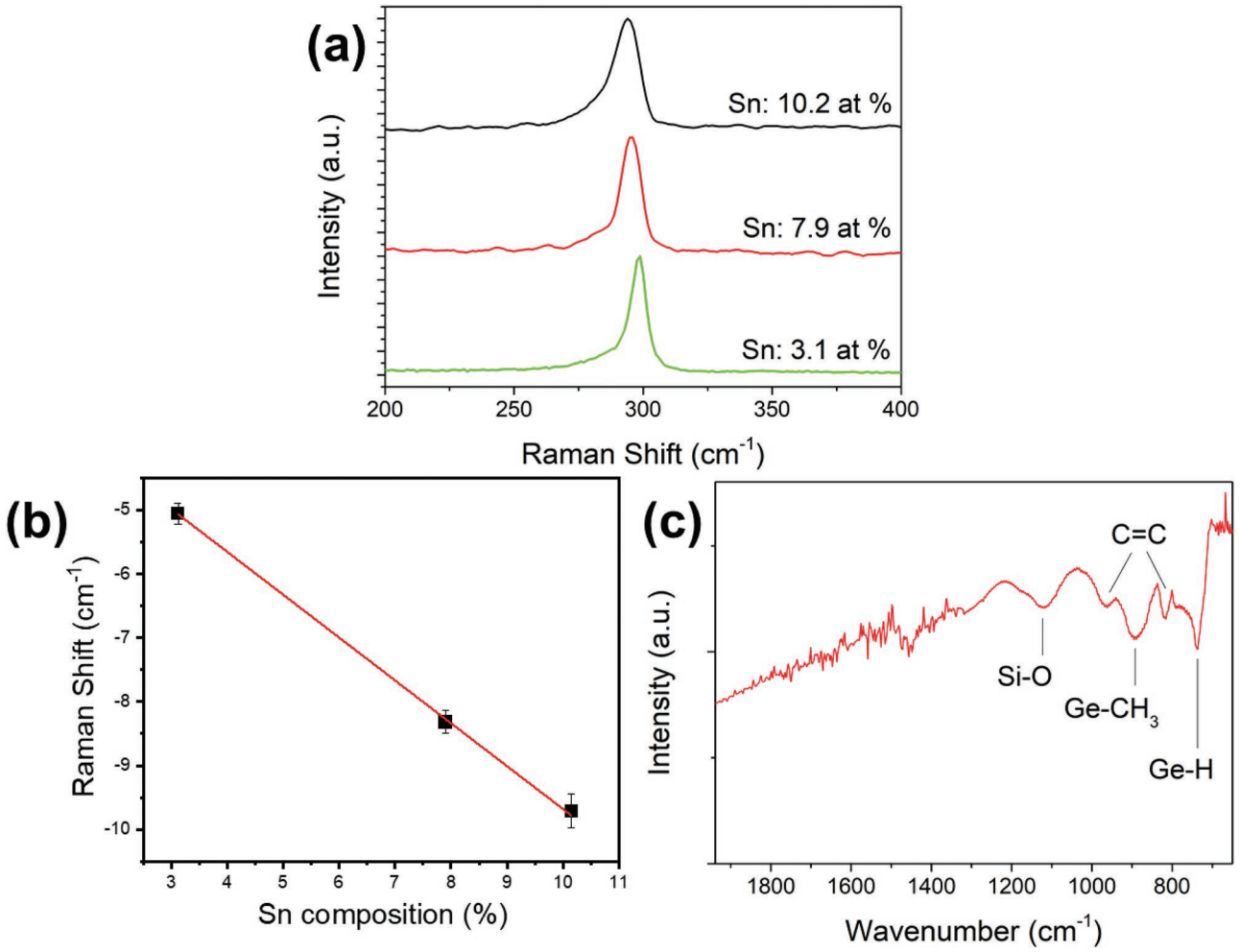

Figure 2. a) Raman spectra of $Ge_{1-x}Sn_x$ nanowires as a function of the average Sn content (at%), within the wave number range of 200–400 cm^{-1}. b) Plotting of the downshift of Ge–Ge LO mode as a function of Sn percentage. Experimental data is represented with dots that fit (straight line) well with the linear expression, $\omega(x) = \omega_0 + \Delta\omega x$. c) FT-IR spectra of the $Ge_{1-x}Sn_x$ nanowires deposited on a Si substrate.

describing the characterized films as completely strain-free. When fitting the Raman peak shift against Sn composition (see Figure 2b) the obtained value for $\Delta\omega$ was found to be $-(69.8 \pm 2.2)$ cm^{-1}, consistent with the previously reported value for strain-free thin film. This linear correlation in the alloy nanowires corroborates the Sn content determined by EDX in the $Ge_{1-x}Sn_x$ nanowires.

The Fourier transform infrared (FTIR) spectra taken from $Ge_{1-x}Sn_x$ ($x = 0.03$) nanowires show absorption bands at ≈750 and ≈890 cm^{-1} (see Figure 2c). These bands have previously been assigned to the wagging mode of Ge–H[45] and Ge–CH_3 rocking vibrations,[46,47] respectively. These data suggest the formation of a carbonaceous structure around the crystalline nanowires due to the presence of peaks at ≈963 and ≈815 cm^{-1}, corresponding to C=C,[46] as well as ≈963 cm^{-1} which is associated with the presence of Ge–C–C.[46,48] These data also suggest a definite interaction of the carbonaceous matrix within the Ge nanowire surfaces. The binary phase diagram of C–Ge alloys implies that the formation of solid solutions of C–Ge is unlikely at the growth temperature of this study.[49] The carbon content detected in the samples arises from the omnipresent adventitious carbon and carbonaceous structures generated during the reaction.

2.2. Structural Characterisation of Nanowires via STEM and HRTEM Analysis

Detail morphology and crystal quality of the nanowires were investigated by HRTEM, HAADF-STEM and selected area electron diffraction (SAED) (see **Figure 3** and Figure S3, Supporting Information). Figure 3a shows HAADF-STEM of representative $Ge_{1-x}Sn_x$ nanowires grown with an initial Ge:Sn mole ratio of 95:5. The TEM image displayed uniform structural quality and a crystalline nature, without any crystal defects such as stacking faults and twinning. Defect-free materials are typically better as Li-ion battery anode materials due to their long life cycles.[50] HRTEM imaging of the nanowires (mean diameter 9.3 nm) revealed an interplanar spacing (d) of 0.33 nm (see Figure 3a) along with a <111> growth direction. The interplanar spacing is marginally larger than the d value reported for bulk dc-Ge (0.326 nm from the JCPDS 04–0545), corresponding to {111}

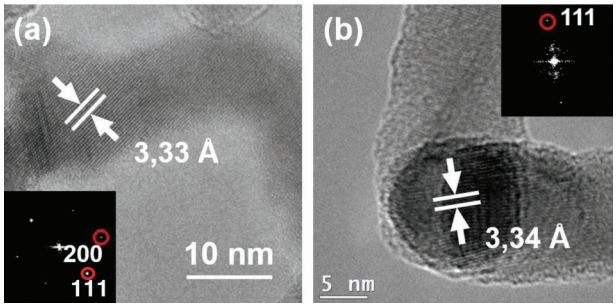

Figure 3. a) Latticed-resolved HRTEM image of a $Ge_{1-x}Sn_x$ nanowire with a mean Sn content of 3.1 at%, revealing an interspace *d* value of 0.333 nm corresponding to the dc-Ge crystal structure. Bottom-left inset shows an FFT of the full image with a corresponding pattern of a representative dc-Ge structure. b) HRTEM image of a Ge/Sn seed. The top-right inset shows an FFT of the full image.

planes of Ge diamond cubic crystal structure. Fast Fourier transform (FFT) analysis of a HAADF-STEM image on a single nanowire could only be indexed to the dc-Ge structure (inset of Figure 3a) and the spot pattern indicates that the Ge nanowires are single-crystalline. Further analysis of the FFT data (inset of Figure 3a) also confirmed the formation of dc-Ge crystal structure and the reflections were assigned to the high-order Laue zone diffraction of two {111} and {200} planes of dc-Ge.[51]

Growth seeds were not readily observed at the tips of the alloy nanowires with the lowest Sn content (3.1 at%). The presence of any observable seeds was further examined by HRTEM (see Figure 3b). Growth seeds with different shapes and nature, in comparison to those formed by a conventional VLS process, were observed in a few instances for these nanowires. Figure 3b shows an HRTEM image of overlapping growth seeds at the tips of two $Ge_{1-x}Sn_x$ nanowires (3.1 at%), confirming the participation of seeded bottom-up growth. The HRTEM image revealed an interplanar spacing (*d*) of 0.34 nm, corresponding to {111} planes of the dc-Ge crystal. HRTEM images show no apparent crystallographic difference between the "seed" and the wire segments. This apparent continuity of the lattice from the seed to the nanowire confirms a VLS-like nanowire growth mechanism, catalyzed from in situ formed Ge nanoparticles. The FFT pattern of the HRTEM image, in the top-right inset of Figure 3b, of the seed region (corresponding to the red-squared area highlighted on the main image) also confirms the formation of the dc-Ge. FFT analysis was recorded from the same nanowire with <110> zone axis alignment. The observation of Ge-rich seeds for low Sn content nanowires is contrary to the observation of Sn-rich (>90 at%) seeds for $Ge_{1-x}Sn_x$ nanowires with a high Sn content, that is, 7.9 and 10.2 at% (see Figure S2, Supporting Information). The observation of Sn-rich seeds is similar to previously reported CVD-grown $Ge_{1-x}Sn_x$ nanowires.[41,42] Shorter and tapered $Ge_{1-x}Sn_x$ nanowires (see Figure S1b, Supporting Information) with a mean Sn content of 7.9 and 10.2 at% clearly display spherical nanoparticle seeds at their tips (see Figures S2a and S3a, Supporting Information). This further suggests two very different growth mechanisms for low and high Sn-content alloy nanowires. High Sn-content (7.9 and 10.2 at%) $Ge_{1-x}Sn_x$ nanowires also depicted a dc-Ge crystal structure, as confirmed by HRSTEM and SAED (see Figure S3b, Supporting Information).

2.3. Growth Mechanism of $Ge_{1-x}Sn_x$ Nanowires

The growth of $Ge_{1-x}Sn_x$ nanowires is believed to occur through a self-seeded supercritical fluid-liquid-solid (SFLS) growth mechanism. The incorporation of Sn in the growing nanowires likely occurs through a solute trapping mechanism.[52] We propose two different growth scenarios for the $Ge_{1-x}Sn_x$ nanowires with low- (3.1 at%) and high-Sn (7.9 and 10.1 at%) content. With low ratios of the Sn precursor in the initial solution $Ge_{1-x}Sn_x$ nanowire growth was initiated by Ge nanoparticle seeds, depicted in the HRTEM image in Figure 3b (see schematic in **Figure 4**a). These Ge nanoparticle seeds were formed by DPG decomposition and stabilized by carbonaceous compounds (formation of carbonaceous structure is confirmed from FTIR in Figure 2c), formed via polymerization of phenyl molecules, liberated as a by-product of DPG decomposition in supercritical toluene atmosphere. These results in $Ge_{1-x}Sn_x$ nanowires with a very thin diameter (9.3 nm) with narrow diameter distribution. The formation of Ge nanoparticle seeds from DPG decomposition seems kinetically favored for the nanowire growth reaction with a 95:5 (Ge:Sn) initial solution. Previously, the growth of $Ge_{1-x}Sn_x$ alloy nanowires with a thin diameter (≈10 nm) and high aspect ratio was seriously hindered by the tendency for Sn to segregate at high concentrations, resulting in thick and short morphologies of $Ge_{1-x}Sn_x$ nanowires. In this work, in situ formation of a carbon-based template is crucial to restrict the Sn agglomeration and achieve nanowires with narrow diameters.

High mole ratios of Sn precursor (TET) in the reaction solution favor homogenous nucleation of Sn and the formation of larger Sn nanoparticle seeds (see Figure 4b), and the growth of $Ge_{1-x}Sn_x$ nanowires with high Sn. The formation of Sn nanoparticles occurs during the Sn precursor decomposition, forming a catalytic seed for nanowire growth. A lack of stabilization of Sn nanoparticles, contrary to the Ge-rich nanoparticle seeds, resulted in thicker nanowires (d = 48.3 and 108.8 nm) with tapered morphology. The inverted and tapered nature of the $Ge_{1-x}Sn_x$ (x = 0.08, 0.10) nanowires grown from an initial solution of 90:10 and 85:15 (Ge:Sn precursors) is caused by the continuous incorporation of Sn adatoms into the catalyst seeds during nanowire growth. A schematic of both growth scenarios is presented in Figure 4.

During the nanowire growth, Sn is incorporated into the nanowire structure at the seed/nanowire interphase.[53] The non-equilibrium incorporation of Sn in the nanowire can be attributed to solute trapping, a kinetically driven process. The difference in atomic concentration of Sn in different phases influences the trapping of Sn adatoms at the triple-phase interface, as previously described.[41,42,52] For the high Sn content nanowire with Sn seed, the large difference in the Sn concentration between the Sn-rich liquid eutectic seed and nanowire can result in the solute trapping of Sn. Additionally, as discussed by Wen et al.,[54] large-diameter nanowires have higher step velocities (growth at the atomic level by step flow) compared to their smaller diameter counterparts, which is also related to a faster impurity trapping rate in the growing nanowires. This higher step velocity in nanowires with larger diameters (d = 48.3 and 108.8 nm) can result in increased Sn% incorporation (7.9 and 10.1 at%).

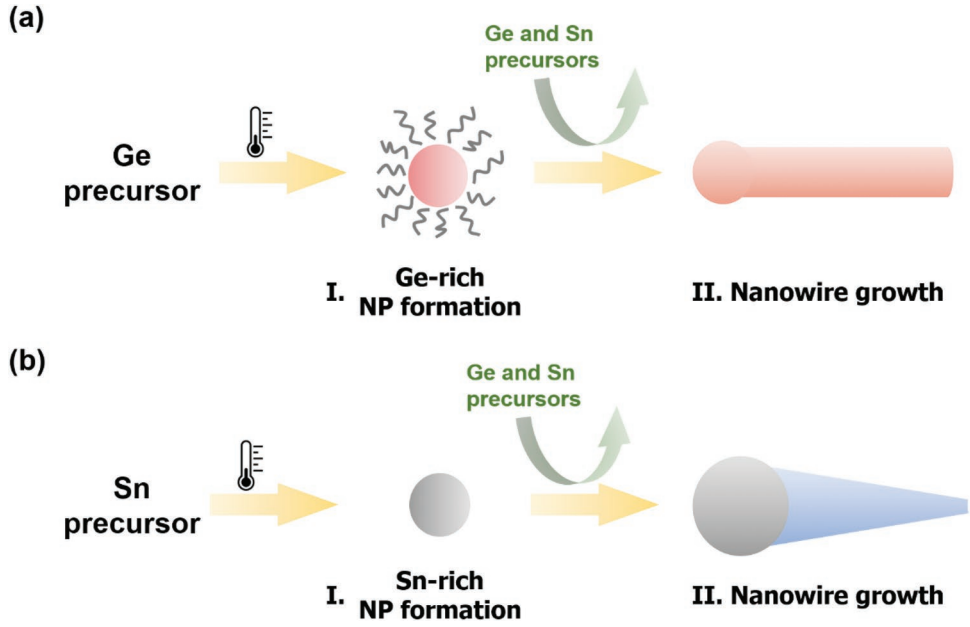

Figure 4. Illustration of the two proposed nanowire growth mechanisms. a) Corresponds to the nanowires (3.1 at% Sn incorporation) grown from an initial solution of 95:5 (Ge:Sn precursors) which generated Ge nanoparticle seed. b) Corresponds to the nanowires (7.9 and 10.1 at% Sn incorporation) grown from initial solutions of 90:10 and 85:15 (Ge:Sn precursors) respectively generating Sn seeds.

2.4. Electrochemical Analysis of $Ge_{1-x}Sn_x$ Nanowires

The morphology and crystal structure of nanowires are tightly related to several Li-ion battery (LIB) variables like the contact area between active material and electrolyte, Li-ions diffusion length, and the area of the SEI film. All these factors influence the electrochemical properties.[55] The motivation to integrate functional materials with high surface areas makes super-thin 3.1 at% Sn containing alloy nanowires good candidates for Li-ion batteries. Besides, as previously shown, $Ge_{1-x}Sn_x$ nanocrystals with high Sn incorporation (≈10 at%) resulted in a decrease in the specific capacity. Metallic Sn tends to segregate, leading to significant side reactions and a decrease in the specific capacity.[27] Therefore, the electrochemical performance of $Ge_{1-x}Sn_x$ nanowires as anodes for LIBs was first tested for the super-thin nanowires with a mean Sn content of 3.1 at%. All $Ge_{1-x}Sn_x$ nanowires were grown directly onto Ti foil current collectors. Nanowires directly grown on current collecting substrates without any additional catalysts do not require initial processing steps, such as decorating the substrate with metal nanoparticle seeds. Also, the use of a binder or conductive additive can be avoided for the nanowires directly grown on current collectors. Further to this, Ti does not participate in nanowire growth (as metal catalysts) at our growth temperatures, unlike Cu foil, in self-seeded $Ge_{1-x}Sn_x$ nanowire

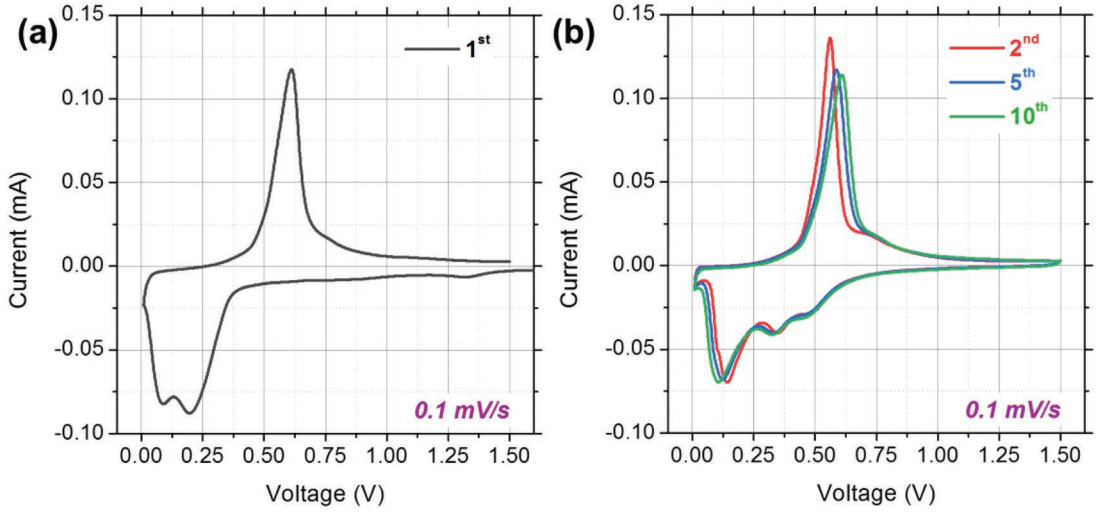

Figure 5. Cyclic voltammograms of $Ge_{1-x}Sn_x$ nanowires with a mean Sn content of 3.1 at.% showing a) the 1st and b) the 2nd, 5th, and 10th cycles; cycled at 0.1 mV s^{-1} in a potential window from 1.5–0.01 V.

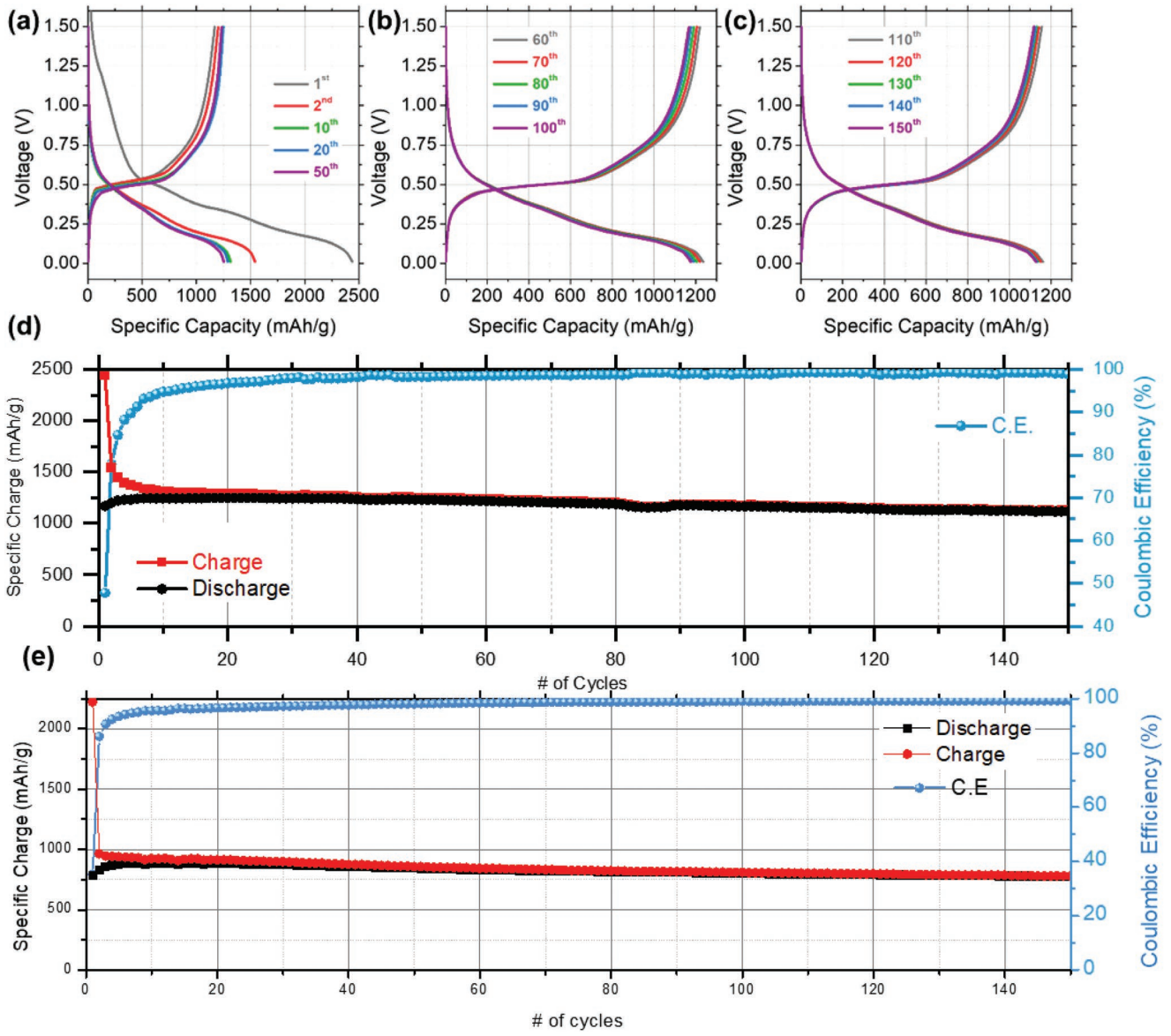

Figure 6. Voltage profiles for a) the 1st, 2nd, 10th, 20th, and 50th cycles, b) the 60th, 70th, 80th, 90th, and 100th cycles, and c) the 110th, 120th, 130th, 140th, and 150th cycles for $Ge_{1-x}Sn_x$ nanowires, with a mean Sn content of 3.1 at%, at 0.2 C in a potential window of 1.50–0.01 V (vs Li/Li^+). d) Specific capacity and Coulombic efficiency values obtained for the same nanowires. e) Specific capacity and Coulombic efficiency values were obtained for the $Ge_{1-x}Sn_x$ nanowires with a mean Sn content of 7.9 at%, at 0.2 C.

growth process. Thus, the nanowires are only composed of Ge and Sn and the variability in the morphological and structural quality of the nanowires is less.

The electrochemical properties of $Ge_{1-x}Sn_x$ nanowires with a mean Sn loading of 3.1 at% were initially investigated by cyclic voltammetry (CV). The first anodic scan (lithiation), (see **Figure 5**a), consisted of a weak reduction peak at ≈0.5 V. This peak is associated with the initial lithiation of crystalline Ge (c-Ge). Whereas, two strong reduction peaks at ≈0.20 and 0.09 V, corresponding to the formation of amorphous and crystalline $Li_{15}Ge_4$ alloys, respectively.[21,56] After this initial lithiation, there is a distinct change in the profile of the reduction peaks observed from the second cycle onwards. Three reduction peaks were observed at ≈0.47, 0.33, and 0.12 V (see Figure 5b), corresponding to the stepwise formation of different Li–Ge alloys (a-Li_xGe → a-$Li_{15}Ge_4$ → c-$Li_{15}Ge_4$).[57] One sharp asymmetric oxidation peak was observed in the cathodic (delithiation) CV scans. The asymmetric nature of this peak indicates that it is a convolution of peaks associated with the delithiation of crystalline and amorphous $Li_{15}Ge_4$ phases.

Galvanostatic cycling of $Ge_{1-x}Sn_x$ nanowires with an Sn content of 3.1. at% was performed to determine the specific capacity values they can deliver and to examine their capacity retention ability. Voltage profiles, observed during galvanostatic cycling at C/5 in a voltage window of 1.5–0.01 V (vs Li/Li^+), are shown in **Figure 6**. This is considered to be a standard rate as it is not very fast or too slow. The relatively low electrical conductivity of Ge and Sn would result in poor electrochemical

performance at fast rates (> 2 C). During the first charge curve (lithiation), the voltage decreased quickly until the initial lithiation of C–Ge commenced at ≈0.5 V, followed by a more gradual decrease to the low voltage limit of 0.01 V, due to the formation of a-$Li_{15}Ge_4$ and c-$Li_{15}Ge_4$ alloys (see Figure 6a). A plateau was observed at ≈0.53 V during the first discharge process (delithiation), corresponding to the dealloying of the nanowires.[19] The specific capacities after the first lithiation and delithiation were 2438 and 1165 mAh g^{-1}, respectively, resulting in initial Coulombic efficiency (ICE) of ≈47. 8%. Low ICE values are commonly reported for alloying mode anode materials and can be attributed to a combination of different factors including, the initial formation of an SEI layer on the surface of the NWs, electrolyte decomposition, and the as well as the formation of quasi reversible Li_2O.[58–61] There was no significant change in the trend of the voltage profiles from the 2nd to the 150th cycle, which indicates that the lithiation of the nanowires is a highly reversible process from the second cycle onwards.

The specific capacity values measured for the nanowires during 150 cycles at 0.2 C, and the corresponding CEs, are shown in Figure 6d. The nanowires demonstrated a high level of capacity retention. The specific capacity after the 10th charge was 1312 mAh g^{-1} and this value decreased gradually to 1176 mAh g^{-1} after the 100th charge and 1127 mAh g^{-1} after the 150th charge. This change corresponds to a capacity retention of ≈90% and 86% from the 10th to the 100th and 150th cycles respectively. The mean capacity decay per cycle from the 2nd cycle onwards was ≈2.8 mAh g^{-1}. The impressive capacity retention of the $Ge_{1-x}Sn_x$ nanowires was also demonstrated in the CE values. After the first 10 cycles, the CE values were > 95% and they remained above this value for the remainder of the 150 cycles.

The redox properties of $Ge_{1-x}Sn_x$ nanowires were further examined through the analysis of differential charge plots (DCPs), which were calculated from galvanostatic cycling curves. The DCP for the first charge (lithiation) consisted of three reduction peaks (see **Figure 7**a), which is in good agreement with the first anodic scan in the CV curves (see Figure 5a). The intensity of the sharp reduction peak associated with the initial lithiation of GeSn, significantly decreased from the second cycle onwards, indicating that after the initial lithiation process, the $Ge_{1-x}Sn_x$ nanowires may not return to a fully delithiated crystalline Ge phase. A similar observation has been reported for other $Ge_{1-x}Sn_x$ nanowires anodes.[26,33] The strong reduction peaks observed at ≈0.35 and 0.18 V can be attributed to the formation of a-$Li_{15}Ge_4$ and c-$Li_{15}Ge_4$ alloys, respectively.[56] The DCP for the first charge (delithiation) consisted of one broad, asymmetric peak which is associated with the delithiation of the c-$Li_{15}Ge_4$ and a-$Li_{15}Ge_4$ phases.

Contour plots were calculated from the DCPs acquired from the 2nd to the 150th cycles (see Figures 7c,d). These contour plots allow the visualization of changes in the intensities of the redox peaks during galvanostatic cycling. The contour plot for the lithiation process (see Figure 7a) demonstrates three reduction peaks at ≈0.50, 0.35, and 0.17 V, corresponding to the formation of amorphous Li–Ge alloys (a-Li_xGe and a-$Li_{15}Ge_4$), and a crystalline Li-Ge alloy (c-$Li_{15}Ge_4$), respectively.[62] The intensity of the reduction peak associated with a-Li_xGe decreases sharply during initial cycling, suggesting that as cycling progresses, less and less of the overall charge stored is due to the formation of this amorphous alloy. The reduction peak associated with the a-$Li_{15}Ge_4$ alloy is observed throughout the 150 cycles, however, the intensity of this peak gradually fades as cycling progressed. Figure 7a shows that the reduction process, which consistently contributes the most towards the overall charge stored, is due to the formation of the c-$Li_{15}Ge_4$ phase. The delithiation contour plot (see Figure 7d) consists of one wide band, centered at ≈0.50 V, which is attributed to the overlapping delithiation of the a-$Li_{15}Ge_4$ and c-$Li_{15}Ge_4$ alloys. Of note, there was no significant shift of the potentials at which the redox process occur during 150 cycles; this stability may contribute to the capacity retention demonstrated in Figure 6d.

With the aim to compare the performance displayed by $Ge_{1-x}Sn_x$ (x = 0.031) nanowires with the higher Sn content, the specific capacity values obtained for the $Ge_{1-x}Sn_x$ nanowires with a mean Sn content of 7.9 at% were measured during 150 cycles at 0.2 C (see Figure 6e). The corresponding voltage profiles are shown in Figure S4, Supporting Information. The specific capacity after the 150th charge was 780 mAh g^{-1}. These nanowires also demonstrated a high level of capacity retention of ≈86% from the 10th to the 150th cycles and a CE after the first 10 cycles > 95% which remained above this value for the remainder of the 150 cycles. $Ge_{1-x}Sn_x$ (x = 0.079) nanowires displayed a significantly lower specific capacity (780 mAh g^{-1} after 150 cycles) in comparison with the $Ge_{1-x}Sn_x$ (x = 0.031) nanowires with long and thin morphology (1127 mAh g^{-1} after 150 cycles) while exhibiting comparable columbic efficiencies. The contrasting battery performance displayed by $Ge_{1-x}Sn_x$ nanowires with different Sn content could be associated with particular morphology and phase purity.

The electrochemical results demonstrated here for the Ge-seeded $Ge_{1-x}Sn_x$ (x = 0.031) nanowires are greater than previously reported capacities for $Ge_{1-x}Sn_x$ alloy-based anodes (Table S1, Supporting Information), and thicker $Ge_{1-x}Sn_x$ (x = 0.079) nanowires grown in this work with in situ formed Sn seed. The $Ge_{1-x}Sn_x$ (x = 0.031) nanowire anode shows the longest cycling stability, compared to other reported work, up to 150 cycles together with the highest reversible capacity (1127 mAh g^{-1}) displayed at a 0.2 C cycling rate. Efficient cycling performance for $Ge_{1-x}Sn_x$ (x = 0.03) nanowires could be attributed to the increased electrical conductivity of the alloy nanowires with homogeneous Sn incorporation in the Ge lattice.[27] There are several factors that contribute to the impressive specific capacity values and stable capacity retention observed, compared to other GeSn nanowires. The growth of the $Ge_{1-x}Sn_x$ (x = 0.03) nanowires was catalyzed via a self-seeded approach (i.e., Ge nanoparticle catalyst). The formation of Li–Sn alloys have previously been observed for $Ge_{1-x}Sn_x$ nanowires which were synthesized with Sn seeds, however, we do not see any contribution from Sn in the DCPs.[56] This is due to the fact that the 3.1 at% Sn incorporated $Ge_{1-x}Sn_x$ nanowires are predominantly seeded by Ge (see Figure 3b), which has a higher theoretical capacity compared to Sn. A low amount of Sn presence in the nanowire bulk and no apparent presence of Sn nanoparticles in the nanowire sample suggests that the formation of any Li–Sn alloys have a negligible contribution towards the overall charge stored. A drop in the specific capacity value was also observed previously in GeSn

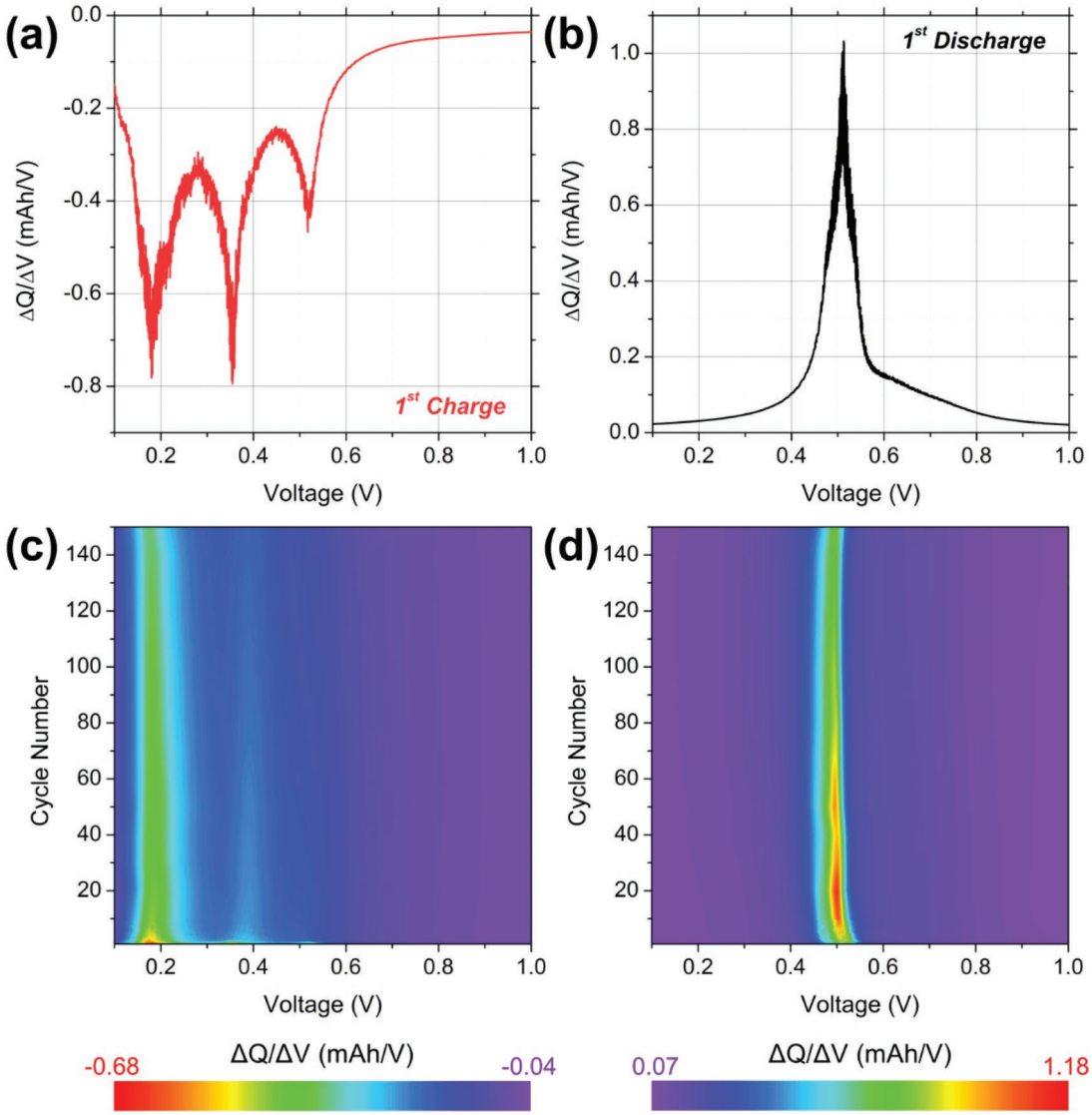

Figure 7. Differential charge plots (DCPs) of $Ge_{1-x}Sn_x$ nanowires (mean Sn content of 3.1 at%) calculated from a) the 1st charge and b) the 1st discharges at 0.2 C. c) Contour DCP calculated from differential charge curves from the 2nd to the 150th charge. d) Contour DCP calculated from differential discharge curves from the 2nd to the 150th discharge.

alloy nanoparticles with higher Sn content (10 at% compared to 5 at%).[27] This was attributed to the presence of metallic Sn-phase, resulting in high charge transfer resistance and lower electrical conductivity. Thus, the high specific capacity for $Ge_{1-x}Sn_x$ (x = 0.03) nanowires compared to the previously reported could be assigned to the absence of any of the metallic Sn (or any other intermetallic) phase at the tip of the nanowires or as segregation and agglomeration. Additionally, very thin nanowire morphology for $Ge_{1-x}Sn_x$ (x = 0.03) nanowires could also contribute to stable and high capacity, as previously reported for Si nanowires.[63] Germanium, like other alloying mode anode materials, is known to undergo significant volume expansion during battery operation. Sn is also an alloying mode material so expansion of regions of the nanowires containing Sn is also likely to occur. Different levels of expansion of Ge and Sn upon lithium insertion is reported previously.[30] It would be difficult to get a very accurate measurement of how much Sn in $Ge_{1-x}Sn_x$ alloy nanowires can better accommodate volume expansion compared to pure Ge nanowires. In situ TEM of pure Ge nanowire sample and $Ge_{1-x}Sn_x$ alloy nanowires may shed some light on this. We have delegated this to a future study.

Additionally, issues associated with the expansion of alloying mode anode materials during lithiation are well documented. However, many reports indicate that nanoparticles under a critical size (diameter ≈200 nm) can better accommodate volume changes without cracking during initial cycles, compared to bulk particles. Consequently, high aspect ratio nanowires with small diameters (≈10 nm) may alleviate issues associated with volume expansion. Very thin $Ge_{1-x}Sn_x$ nanowires could also implement a shorter diffusion pathway for lithium, ensuring a fast and homogeneous lithiation. Amorphous carbon coating

in $Ge_{1-x}Sn_x$ ($x = 0.03$) nanowires can also positively influence specific capacity and capacity retention. The presence of carbon coatings will drastically enhance the reaction kinetics during cycles by promoting electron transport, increasing electrical contact points, and providing more paths for charge carrier transfer.[64] Significantly, $Ge_{1-x}Sn_x$ nanowires are grown directly on a Ti substrate, ensuring that the nanowires are in intimate contact with the current collector. Growing $Ge_{1-x}Sn_x$ nanowires directly on a current collector also negates the need to prepare a traditional slurry with a conductive additive and binder. The stable capacity retention shown in Figure 6d is impressive as it was achieved without the need to prepare slurry-based electrodes. Additionally, rational electrode design[65–67] is needed to improve the performance of anode based on novel materials like $Ge_{1-x}Sn_x$ nanowires.

3. Conclusion

In summary, an alternative and simple bottom-up method was developed for the growth $Ge_{1-x}Sn_x$ nanowires that could potentially be used as an anode material in Li-ion batteries. These alloy nanowires were successfully grown directly on titanium substrates, which act as anode current collectors, eliminating the need for conductive slurry and binders. The simple and versatile solvothermal-like growth method does not require any catalyst metal seeds, templates, designer precursors, or high boiling point solvents. Sn incorporation into the Ge lattice was achieved between 3.1 to 10.2 at%. A distinct change in the morphology of the nanowires and growth seeds was observed for $Ge_{1-x}Sn_x$ nanowires with different Sn content. $Ge_{1-x}Sn_x$ nanowires with 3.1 at.% Sn incorporation are very thin (mean diameter of 9.3 nm) and long, whereas thicker, shorter, and tapered (mean diameter of 48.3 and 108.8 nm) nanowires were observed for larger (≈8%–10%) Sn incorporation.

$Ge_{1-x}Sn_x$ nanowires with a mean Sn content of 3.1 at% demonstrated good performance as Li-ion battery anodes. The nanowires exhibited a high level of capacity retention, with a reversible specific capacity of 1127 mAh g^{-1} after the 150th charge, when cycled at 0.2 C. The impressive capacity retention of the nanowires was highlighted by the mean capacity decay per cycle of just ≈2.8 mAh g^{-1} from the 2nd to the 150th cycle. Analysis of differential charge plots revealed that the formation of a-$Li_{15}Ge_4$ and c-$Li_{15}Ge_4$ alloys are highly reversible and that the majority of the charge stored is due to the reduction process associated with the development of the c-$Li_{15}Ge_4$ phase. The high specific capacity values obtained for the nanowires surpassed previously reported values for GeSn alloy-based anodes. This work also highlights the significance of utilizing phase pure, that is, without any presence of metallic Sn, and superthin GeSn nanowires as LIB anode. The impressive electrochemical performance of the $Ge_{1-x}Sn_x$ ($x = 0.031$) nanowires in terms of specific capacities, Coulombic efficiency, and voltage stability demonstrates that they are a promising anode material for advanced Li-ion batteries. A future goal could be to achieve and utilize Ge-seeded $Ge_{1-x}Sn_x$ nanowires with higher Sn content in Li-ion batteries.

4. Experimental Section

Anhydrous toluene (99.8%) was purchased from Sigma-Aldrich Co, diphenylgermane (DPG) 95% was purchased from Fluorochem, and tetraethyltin (TET) 97% was purchased from Alpha Aesar. All chemicals were stored and used under N_2 in a glovebox ($O_2 < 0.1$ ppm, $H_2O < 0.5$ ppm).

$Ge_{1-x}Sn_x$ nanowire synthesis was carried out in a 1 mL stainless steel reaction cell. Prior to synthesis, the reaction cell and connectors were dried under vacuum at 125 °C for 12 h. Reactions were performed at a temperature of 440 °C on Ti foil disk substrates (0.6 cm in diameter, native oxide present). The reaction temperature was monitored using a thermocouple connected to the reaction vessel and the pressure was monitored via a pressure gauge, connected to one end of the reaction cell. In general, 0.6 ml of a toluene/DPG/TET solution was added to the 1 ml reaction cell and the cell was heated to the desired temperature in a tube furnace for 60 min. The DPG/TET concentration varied between 20/1, 20/2, 20/4, and 20/7 mM, which corresponded to mole ratios of 95:5, 90:10, 85:15, and 75:25. The filling volume of the reactant solution, that is, filling fraction, was 60% of the total reactor's volume (1 ml). The reaction cell was cooled to room temperature after the reaction and disassembled to access the growth substrate. Growth substrates were washed with dry toluene and dried under an N_2 flow for further characterization.

Structural and Chemical Characterization: Samples were imaged using an FEI Quanta FEG 650 scanning electron microscope (SEM) operated at 15 kV. High-resolution transmission electron microscopy (HRTEM) and high-resolution scanning transmission electron microscopy (HRSTEM) imaging were performed on a JEOL 2100 electron microscope operated at 200 kV and an FEI Titan electron microscope, operating at 300 kV. High-angle annular-dark-field scanning-transmission-electron-microscopy (HAADF-STEM) was performed on the FEI Titan electron microscope operated at 300 kV. Raman scattering analysis was performed using a Lab RAM HR (Jobin Yvon) spectrometer equipped with a 488 nm laser source and a CCD detector. The laser was focused on the sample using a 100× objective lens. The laser power was maintained at 0.18 mW throughout the measurement and the data acquisition time was 50 s. Raman scattering analysis was performed on the nanowires at low power (0.18 mW); to avoid laser-induced heating which can cause structural changes in the nanowires and a red-shift in the Ge–Ge phonon vibration. Raman spectra for the nanowires were recorded over a wave number range between 200–400 cm^{-1}. Fourier-transform infrared spectroscopy (FTIR) spectra were recorded on a Varian IR 660 infrared spectrometer between the wavelength range of 400 to 4000 cm^{-1}.

The electrochemical properties of $Ge_{1-x}Sn_x$ nanowire anodes were investigated in two electrode Swagelok cells assembled in an Ar-filled glovebox. $Ge_{1-x}Sn_x$ nanowire anodes were cycled against pure Li metal counter electrodes. Electrochemical tests were performed using a BioLogic VSP Potentiostat/Galvanostat. The electrolyte was a 1 mol dm^{-3} solution of $LiPF_6$ in a 1:1 (v/v) mixture of ethylene carbonate in dimethyl carbonate with 3 wt% vinylene carbonate; 200 µL of electrolyte was used in each cell. The separator used in all electrochemical tests was Celgard 2400 (diameter: 13 mm, thickness: 25 µm). A Mettler Toledo XP2U ultra microbalance was used to determine the mass of $Ge_{1-x}Sn_x$ nanowires on the Ti foil substrates. The size of the Ti foil substrates was 0.5 × 1.0 cm, therefore the areal mass loading of the $Ge_{1-x}Sn_x$ nanowires on the stainless-steel current collectors was 3.45 µg mm^{-2}. Cyclic voltammetry was performed at a scan rate of 0.1 mV s^{-1} in a potential window of 1.5–0.01 V (vs Li/Li^+). Galvanostatic cycling was performed at 0.2 C in a potential window of 1.5–0.01 V (vs Li/Li^+).

Supporting Information

Supporting Information is available from the Wiley Online Library or from the author.

Acknowledgements

This research was funded by Science Foundation Ireland (Grant No: 14/IA/2513). A part of the imaging for this project was carried out at the Advanced Microscopy Laboratory (AML) at the AMBER Centre, CRANN Institute, Trinity College Dublin, Ireland. AML is an SFI supported Imaging and Analysis Centre.

Open access funding provided by IReL.

Conflict of Interest

The authors declare no conflict of interest.

Authors Contribution

A.G and S.B contributed equally as first author.

Data Availability Statement

The data that support the findings of this study are available from the corresponding author upon reasonable request.

Keywords

germanium-tin nanowires, Li-ion battery anode, supercritical growth conditions, super-thin nanowires

Received: May 26, 2022
Revised: July 4, 2022
Published online: September 7, 2022

[1] J. Doherty, S. Biswas, E. Galluccio, C. A. Broderick, A. Garcia-Gil, R. Duffy, E. P. O'Reilly, J. D. Holmes, *Chem. Mater.* **2020**, *32*, 4383.
[2] N. Uchida, T. Maeda, R. R. Lieten, S. Okajima, Y. Ohishi, R. Takase, M. Ishimaru, J. P. Locquet, *Appl. Phys. Lett.* **2015**, *107*, 232105.
[3] J. D. Sau, M. L. Cohen, *Phys. Rev. B: Condens. Matter Mater. Phys.* **2007**, *75*, 045208.
[4] R. R. Lieten, T. Maeda, W. Jevasuwan, H. Hattori, N. Uchida, S. Miura, M. Tanaka, J. P. Locquet, *Appl. Phys. Express* **2013**, *6*, 101301.
[5] H. Cong, F. Yang, C. Xue, K. Yu, L. Zhou, N. Wang, B. Cheng, Q. Wang, *Small* **2018**, *14*, 1704414.
[6] W. J. Yin, X. G. Gong, S. H. Wei, *Phys. Rev. B: Condens. Matter Mater. Phys.* **2008**, *78*, 161203.
[7] R. Chen, H. Lin, Y. Huo, C. Hitzman, T. I. Kamins, J. S. Harris, *Appl. Phys. Lett.* **2011**, *99*, 181125.
[8] E. Azrak, W. Chen, S. Moldovan, S. Gao, S. Duguay, P. Pareige, P. R. I. Cabarrocas, *J. Phys. Chem. C* **2018**, *122*, 26236.
[9] S. Wirths, R. Geiger, N. Von Den Driesch, G. Mussler, T. Stoica, S. Mantl, Z. Ikonic, M. Luysberg, S. Chiussi, J. M. Hartmann, H. Sigg, J. Faist, D. Buca, D. Grützmacher, *Nat. Photonics* **2015**, *9*, 88.
[10] D. Stange, S. Wirths, R. Geiger, C. Schulte-Braucks, B. Marzban, N. V. Den Driesch, G. Mussler, T. Zabel, T. Stoica, J. M. Hartmann, S. Mantl, Z. Ikonic, D. Grützmacher, H. Sigg, J. Witzens, D. Buca, *ACS Photonics* **2016**, *3*, 1279.
[11] S. Al-Kabi, S. A. Ghetmiri, J. Margetis, T. Pham, Y. Zhou, W. Dou, B. Collier, R. Quinde, W. Du, A. Mosleh, J. Liu, G. Sun, R. A. Soref, J. Tolle, B. Li, M. Mortazavi, H. A. Naseem, S. Q. Yu, *Appl. Phys. Lett.* **2016**, *109*, 171105.
[12] B. R. Conley, J. Margetis, W. Du, H. Tran, A. Mosleh, S. A. Ghetmiri, J. Tolle, G. Sun, R. Soref, B. Li, H. A. Naseem, S. Q. Yu, *Appl. Phys. Lett.* **2014**, *105*, 221117.
[13] T. N. Pham, W. Du, B. R. Conley, J. Margetis, G. Sun, R. A. Soref, J. Tolle, B. Li, S. Q. Yu, *Electron. Lett.* **2015**, *51*, 854.
[14] H. H. Tseng, K. Y. Wu, H. Li, V. Mashanov, H. H. Cheng, G. Sun, R. A. Soref, *Appl. Phys. Lett.* **2013**, *102*, 182106.
[15] J. P. Gupta, N. Bhargava, S. Kim, T. Adam, J. Kolodzey, *Appl. Phys. Lett.* **2013**, *102*, 251117.
[16] C. Chang, T. W. Chang, H. Li, H. H. Cheng, R. Soref, G. Sun, J. R. Hendrickson, *Appl. Phys. Lett.* **2017**, *111*, 141105.
[17] A. M. Ionescu, H. Riel, *Nature* **2011**, *479*, 329.
[18] Q. T. Zhao, S. Richter, C. Schulte-Braucks, L. Knoll, S. Blaeser, G. V. Luong, S. Trellenkamp, A. Schafer, A. Tiedemann, J. M. Hartmann, K. Bourdelle, S. Mantl, *IEEE J. Electron Devices Soc.* **2015**, *3*, 103.
[19] D. McNulty, S. Biswas, S. Garvey, C. O'Dwyer, J. D. Holmes, *ACS Appl. Energy Mater.* **2020**, *3*, 11811.
[20] E. Mullane, T. Kennedy, H. Geaney, C. Dickinson, K. M. Ryan, *Chem. Mater.* **2013**, *25*, 1816.
[21] E. Mullane, T. Kennedy, H. Geaney, K. M. Ryan, *ACS Appl. Mater. Interfaces* **2014**, *6*, 18800.
[22] X. Liu, X. Y. Wu, B. Chang, K. X. Wang, *Energy Storage Mater.* **2020**, *30*, 146.
[23] H. Tian, F. Xin, X. Wang, W. He, W. Han, *J. Materiomics* **2015**, *1*, 153.
[24] S. Chu, A. Majumdar, *Nature* **2012**, *488*, 294.
[25] S. Yoon, C. M. Park, H. J. Sohn, *Electrochem. Solid-State Lett.* **2008**, *11*, A42.
[26] J. Doherty, D. McNulty, S. Biswas, K. Moore, M. Conroy, U. Bangert, C. O'Dwyer, J. D. Holmes, *Nanotechnology* **2020**, *31*, 165402.
[27] Y. J. Cho, C. H. Kim, H. S. Im, Y. Myung, H. S. Kim, S. H. Back, Y. R. Lim, C. S. Jung, D. M. Jang, J. Park, S. H. Lim, E. H. Cha, K. Y. Bae, M. S. Song, W. Il Cho, *Phys. Chem. Chem. Phys.* **2013**, *15*, 11691.
[28] H. Lee, J. Cho, *Nano Lett.* **2007**, *7*, 2638.
[29] M. G. Kim, J. Cho, *J. Electrochem. Soc.* **2009**, *156*, A277.
[30] C. Y. Chou, H. Kim, G. S. Hwang, *J. Phys. Chem. C* **2011**, *115*, 20018.
[31] G. H. Lee, S. J. Kwon, K. S. Park, J. G. Kang, J. G. Park, S. Lee, J. C. Kim, H. W. Shim, D. W. Kim, *Sci. Rep.* **2014**, *4*, 6883.
[32] H. Lee, M. G. Kim, C. H. Choi, Y. K. Sun, C. S. Yoon, J. Cho, *J. Phys. Chem. B* **2005**, *109*, 20719.
[33] J. Doherty, S. Biswas, D. Mcnulty, C. Downing, S. Raha, C. O. Regan, A. Singha, C. O. Dwyer, J. D. Holmes, *Chem. Mater.* **2019**, *31*, 4016.
[34] M. H. Park, Y. Cho, K. Kim, J. Kim, M. Liu, J. Cho, *Angew. Chem., Int. Ed.* **2011**, *50*, 9647.
[35] M. R. Zamfir, H. T. Nguyen, E. Moyen, Y. H. Lee, D. Pribat, *J. Mater. Chem. A* **2013**, *1*, 9566.
[36] T. Haffner, M. Zeghouane, F. Bassani, P. Gentile, A. Gassenq, F. Chouchane, N. Pauc, E. Martinez, E. Robin, S. David, T. Baron, B. Salem, *Phys. Status Solidi A* **2017**, *215*, 1700743.
[37] M. S. Seifner, S. Hernandez, J. Bernardi, A. Romano-Rodriguez, S. Barth, *Chem. Mater.* **2017**, *29*, 9802.
[38] S. Barth, S. Seifner, J. Bernardi, *Chem. Commun.* **2015**, *51*, 12282.
[39] Y. L. Sun, R. Matsumura, W. Jevasuwan, N. Fukata, *Nano Lett.* **2019**, *19*, 6270.
[40] F. W. Yuan, H. J. Yang, H. Y. Tuan, *J. Mater. Chem.* **2011**, *21*, 13793.
[41] S. Biswas, J. Doherty, D. Saladukha, Q. Ramasse, D. Majumdar, M. Upmanyu, A. Singha, T. Ochalski, M. A. Morris, J. D. Holmes, *Nat. Commun.* **2016**, *7*, 114005.
[42] J. Doherty, S. Biswas, D. Saladukha, Q. Ramasse, T. S. Bhattacharya, A. Singha, T. J. Ochalski, J. D. Holmes, *J. Mater. Chem. C* **2018**, *6*, 8738.
[43] S. Su, W. Wang, B. Cheng, W. Hu, G. Zhang, C. Xue, Y. Zuo, Q. Wang, *Solid State Commun.* **2011**, *151*, 647.
[44] S. F. Li, M. R. Bauer, J. Menéndez, J. Kouvetakis, *Appl. Phys. Lett.* **2004**, *84*, 867.
[45] M. Cardona, *Phys. Status Solidi B* **1983**, *118*, 463.
[46] P. Kazimierski, Ł. Jóźwiak, *J. Non-Cryst. Solids* **2009**, *355*, 280.

[47] M. Gazicki, *Chaos, Solitons Fractals* **1999**, *10*, 1983.
[48] J. Tyczkowski, P. Kazimierski, H. Szymanowski, *Thin Solid Films* **1994**, *241*, 291.
[49] R. I. Scace, G. A. Slack, *J. Chem. Phys.* **1959**, *30*, 1551.
[50] K. H. Park, D. Lee, J. Kim, J. Song, Y. M. Lee, H. T. Kim, J. K. Park, *Nano Lett.* **2014**, *14*, 4306.
[51] D. C. Bell, Y. Wu, C. J. Barrelet, S. Gradeč Ak, J. Xiang, B. P. Timko, C. M. Lieber, *Microsc. Res. Tech.* **2004**, *64*, 373.
[52] O. Moutanabbir, D. Isheim, H. Blumtritt, S. Senz, E. Pippel, D. N. Seidman, *Nature* **2013**, *496*, 78.
[53] B. A. Wacaser, K. A. Dick, J. Johansson, M. T. Borgström, K. Deppert, L. Samuelson, *Adv. Mater.* **2009**, *21*, 153.
[54] C. Y. Wen, J. Tersoff, M. C. Reuter, E. A. Stach, F. M. Ross, *Phys. Rev. Lett.* **2010**, *105*, 195502.
[55] J. Y. Xiang, J. P. Tu, L. Zhang, Y. Zhou, X. L. Wang, S. J. Shi, *J. Power Sources* **2010**, *195*, 313.
[56] T. Kennedy, E. Mullane, H. Geaney, M. Osiak, C. O'Dwyer, K. M. Ryan, *Nano Lett.* **2014**, *14*, 716.
[57] L. Baggetto, P. H. L. Notten, *J. Electrochem. Soc.* **2009**, *156*, A169.
[58] G. T. Kim, T. Kennedy, M. Brandon, H. Geaney, K. M. Ryan, S. Passerini, G. B. Appetecchi, *ACS Nano* **2017**, *11*, 5933.
[59] A. M. Chockla, K. C. Klavetter, C. B. Mullins, B. A. Korgel, *ACS Appl. Mater. Interfaces* **2012**, *4*, 4658.
[60] D. McNulty, H. Geaney, Q. Ramasse, C. O'Dwyer, *Adv. Funct. Mater.* **2020**, *30*, 2005073.
[61] D. McNulty, H. Geaney, D. Buckley, C. O'Dwyer, *Nano Energy* **2018**, *43*, 11.
[62] X. H. Liu, S. Huang, S. T. Picraux, J. Li, T. Zhu, J. Y. Huang, *Nano Lett.* **2011**, *11*, 3991.
[63] A. Gohier, B. Laïk, J. P. Pereira-Ramos, C. S. Cojocaru, P. Tran-Van, *J. Power Sources* **2012**, *203*, 135.
[64] X. H. Liu, L. Q. Zhang, L. Zhong, Y. Liu, H. Zheng, J. W. Wang, J. H. Cho, S. A. Dayeh, S. T. Picraux, J. P. Sullivan, S. X. Mao, Z. Z. Ye, J. Y. Huang, *Nano Lett.* **2011**, *11*, 2251.
[65] H. Li, H. Wang, D. Chan, Z. Xu, K. Wang, M. Ge, Y. Zhang, S. Chen, Y. Tang, *Carbon Energy* **2022**, https://doi.org/10.1002/CEY2.187.
[66] M. Chen, Y. Zhang, G. Xing, S. L. Chou, Y. Tang, *Energy Environ. Sci.* **2021**, *14*, 3323.
[67] J. Zhao, H. Lu, Y. Zhang, S. Yu, O. I. Malyi, X. Zhao, L. Wang, H. Wang, J. Peng, X. Li, Y. Zhang, S. Chen, H. Pan, G. Xing, C. Lu, Y. Tang, X. Chen, *Sci. Adv.* **2021**, *7*, https://doi.org/10.1126/sciadv.abd6978.